

Synthesis of an Ultradense Forest of Vertically Aligned Triple-Walled Carbon Nanotubes of Uniform Diameter and Length Using Hollow Catalytic Nanoparticles

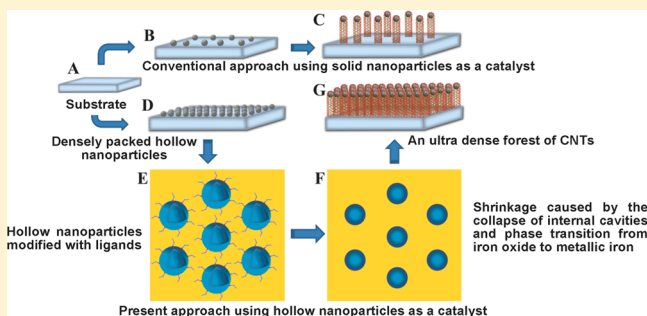
Ankur Baliyan,[†] Yoshikata Nakajima,^{†,§} Takahiro Fukuda,[†] Takashi Uchida,^{†,§} Tatsuro Hanajiri,^{†,§} and Toru Maekawa^{*,†,§}

[†]Bio-Nano Electronics Research Centre, Toyo University 2100, Kujirai, Kawagoe, Saitama 350-8585, Japan

[§]Graduate School of Interdisciplinary New Science, Toyo University 2100, Kujirai, Kawagoe, Saitama 350-8585, Japan

Supporting Information

ABSTRACT: It still remains a crucial challenge to actively control carbon nanotube (CNT) structure such as the alignment, area density, diameter, length, chirality, and number of walls. Here, we synthesize an ultradense forest of CNTs of a uniform internal diameter by the plasma-enhanced chemical vapor deposition (PECVD) method using hollow nanoparticles (HNPs) modified with ligand as a catalyst. The diameters of the HNPs and internal cavities in the HNPs are uniform. A monolayer of densely packed HNPs is self-assembled on a silicon substrate by spin coating. HNPs shrink via the collapse of the internal cavities and phase transition from iron oxide to metallic iron in hydrogen plasma during the PECVD process. Agglomeration of catalytic NPs is avoided on account of the shrinkage of the NPs and ligand attached to the NPs. Diffusion of NPs into the substrate, which would inactivate the growth of CNTs, is also avoided on account of the ligand. As a result, an ultradense forest of triple-walled CNTs of a uniform internal diameter is successfully synthesized. The area density of the grown CNTs is as high as $0.6 \times 10^{12} \text{ cm}^{-2}$. Finally, the activity of the catalytic NPs and the NP/carbon interactions during the growth process of CNTs are investigated and discussed. We believe that the present approach may make a great contribution to the development of an innovative synthetic method for CNTs with selective properties.



1. INTRODUCTION

Almost two decades have passed since the race for the synthesis of carbon nanotubes (CNTs) started, and remarkable progress has been made in the development of innovative synthetic methodologies for growing high quality CNTs with specific properties. Best practices are now recognized and shared worldwide. However, it still remains a crucial challenge to actively control carbon nanotube structure such as the alignment, area density, diameter, length, chirality, and number of walls. The properties of CNTs are structure sensitive and highly dependent on the above structural aspects. There are several reports which show that the diameter, length, alignment, and number of walls of CNTs are strongly influenced by the size of catalytic nanoparticles (NPs).^{1–5} However, there are only a few reports on simultaneous control of both the structural aspects and area density of grown CNTs.^{6–8} The obvious constraints in the existing process on the control of the structural aspects and area density of CNTs are (a) precise control over the size of catalytic NPs and (b) architectural arrangement of catalytic NPs on a desired substrate without aggregations. An ideal scenario can be visualized as follows: (a) the size of the catalytic NPs should be uniform enough to produce monodisperse CNTs and (b) the distance between

NPs should be as minimal as possible without aggregations at elevated temperature. The formation of a densely packed long-range self-assembled monolayer of monodisperse catalytic NPs on substrates without aggregation is a best solution for the growth of an ultradense forest of vertically aligned CNTs (V-CNTs) of uniform internal diameters and lengths.

Recent efforts include heat treatment of thin metal films,⁹ attachment of block copolymer micelles to the surface of NPs,⁸ and employment of liquid-phase catalytic NPs.¹⁰ Reproducibility, precise control over the diameter, area density, and number of walls, and cost effectiveness are the major issues associated with the above methods. Thin metal film deposition is widely accepted but suffers from the inability to have specific control over the size and arrangement of NPs. It is also quite an expensive technique. The size, area density, and chemical state of NPs are dependent on the process parameters.⁶ The size and arrangement of NPs significantly vary during annealing of the deposited thin film, which is again a main drawback. Copolymer micelles can control the size and area density of NPs, but the catalytic activity is very low. Therefore,

Received: October 22, 2013

Published: December 25, 2013

preprocessing such as prolonged annealing is necessary to enhance the catalytic activity, in which case copolymers coated on the surface of NPs would be detached and, as a result, polydisperse CNTs are likely to be grown. The process also suffers from the inability for mass production. One promising solution is to use premade monodisperse NPs because the employment of monodisperse NPs as a catalyst to grow CNTs of selective diameters has gained momentum.^{1,4,10–12} Use of premade monodisperse NPs as a catalyst has several advantages: (a) its scalability to a large quantity of NPs while maintaining a narrow size distribution; (b) its ability to form a dense long-range self-assembled monolayer on desired substrates; (c) reduction of a number of parameters involved in the entire growth process of CNTs.^{1,4} However, the low catalytic activity and agglomeration of NPs become crucial problems at elevated temperature.¹³ The above ideal scenario for the growth of ultradense, vertically aligned CNTs of uniform diameter and length requires truly innovative technique for synthesizing catalytic NPs.

Here, we devise an alternative route to the growth of an ultradense forest of vertically aligned triple-walled carbon nanotubes (V-TWNTs) of a selective diameter by replacing the conventional solid NPs with engineered monodisperse hollow nanoparticles (HNPs) as a catalyst. An ultradense forest of V-TWNTs of a uniform diameter is grown by the plasma-enhanced chemical vapor deposition (PECVD) method using the monodisperse HNPs. We demonstrate that monodisperse HNPs shrink toward the center, which consequently makes the interparticle distance longer, by which the agglomeration among the NPs can be avoided even at elevated temperature. As per our knowledge, the synthesis of TWNTs of such a high area density as $0.6 \times 10^{12} \text{ cm}^{-2}$ has not yet been achieved. What is more, the present methodology does not require any additional process to improve the catalytic activity. The structural stability and purity of the TWNTs are thoroughly investigated. We also highlight the primary factors, which affect the catalytic activity of NPs. Noting that TWNTs are of great importance for the design and development of nanobearing and nanogear-based complex nanodevices, the present approach may well make a great contribution to the development of an efficient synthetic methodology for highly selective CNTs.

2. EXPERIMENTAL METHODS

2.1. Synthesis of Hollow Fe_3O_4 Nanoparticles. Monodisperse HNPs were synthesized by the modified facile solution-phase process, controlling oxidation of the amorphous core/shell $\text{Fe}/\text{Fe}_3\text{O}_4$ NPs. There are two steps in the modified facile synthesis: (a) synthesis of amorphous core/shell $\text{Fe}/\text{Fe}_3\text{O}_4$ NPs; (b) synthesis of crystalline Fe_3O_4 HNPs by the control of oxidation of amorphous core/shell $\text{Fe}/\text{Fe}_3\text{O}_4$ NPs.^{14,15}

2.1.1. Synthesis of Core/Shell Nanoparticles. 1-Octadecene (20.0 mL) and oleylamine (0.2 mL) were mixed and degassed at 120 °C for 30 min to remove the moisture and trapped oxygen. Under argon atmosphere, the solution temperature was increased up to 180 °C, and 0.7 mL of iron pentacarbonyl was quickly injected into the mixture under vigorous stirring, followed by oleic acid (0.05 mL). Immediately after the injection of iron precursor, the solution color started to change. The temperature of the solution was kept at 180 °C for 30 min, and then the solution was cooled to room temperature. Further processing was performed in a N_2 protection glovebox: (a) the supernatant was discarded and (b) the black product was washed three to four times using ethanol and centrifuged before being finally dispersed in *n*-hexane.

2.1.2. Synthesis of Hollow Catalytic Nanoparticles. 1-Octadecene (20.0 mL) and trimethylamine *N*-oxide (35.0 mg) were mixed for 30

min under argon atmosphere. A 50 mg mL^{-1} solution of NPs in *n*-hexane was injected into the mixture under vigorous stirring at 120 °C for 1.5 h to remove the excess *n*-hexane, and the solution was kept at 180 °C for 1.5 h for oxidation before being cooled to room temperature. Further processing was carried out under normal atmosphere: (a) the supernatant was discarded and (b) excess trimethylamine *N*-oxide and other impurities were washed repeatedly three to four times using ethanol and centrifuged. The black final product; i.e., HNPs, was dispersed in *n*-hexane (0.04 mg mL^{-1}) and stored in glass vials at 4 °C in a refrigerator for further use.

2.2. Deposition and Characterization of Hollow Fe_3O_4 Nanoparticles.

Silicon substrates were cleaned using acetone, and 100 μL of the solution of monodisperse HNPs dispersed in *n*-hexane was spin coated over a silicon substrate of $2.54 \times 2.54 \text{ cm}^2$ at 2000 rpm. The size distribution and structures of NPs were characterized by a transmission electron microscope (TEM) (JEM2300-F, JEOL). The chemical composition of NPs was ascertained by energy-dispersive X-ray spectroscopy (EDS) (JED2300-T, JEOL). X-ray diffraction (XRD) patterns of the particles' assemblies were analyzed by an X-ray diffractometer (Rigaku-RINT). Fourier transform infrared (FTIR) spectra of dried NPs were measured (FT-IR spectrum 100, PerkinElmer, Inc.). The surface morphology of NPs deposited on silicon substrates was characterized by a high-resolution scanning electron microscope (HRSEM) (SU8030, Hitachi) and an atomic force microscope (AFM) in noncontact mode (MFP-3D-CF, Asylum Research). A super sharp tip with a radius of less than 5.0 nm was used for surface imaging (Nanosensors, Asylum Research). Thermogravimetric analysis (TGA) of dried NPs was performed (DTG-60H, Shimadzu Scientific Instruments). Inward diffusion of NPs into a silicon matrix was characterized by secondary ion mass spectroscopy (SIMS) (TOFSIMS, ION-TOF GmbH).

2.3. Synthesis and Characterization of Carbon Nanotubes. A plasma-enhanced chemical vapor deposition (PECVD) setup (ULVAC, Inc.) was used for the synthesis of V-CNTs. The schematic diagram of the setup is shown in ref 5. A silicon substrate, on which nanoparticles had been deposited, was mounted on the substrate holder. A negatively biased voltage of 10 V was applied between the substrate and mesh. The microwave power was set at 350 W for the generation of plasma. The substrate was heated up to 650 °C at an increase rate of 100 °C min^{-1} with a H_2 flow at 20 standard cubic centimeters per minute (sccm). As soon as the substrate temperature reached 400 °C, hydrogen plasma was switched on. Then, H_2 and CH_4 gases were introduced into the chamber at a flow rate of 80 and 20 sccm, respectively, for 10 min. The pressure was maintained at 5.0 Torr (666.65 Pa) during the entire process. Finally, the system was cooled in a nitrogen atmosphere. The surface morphologies of CNTs were studied using a high-resolution scanning electron microscope (HRSEM) (SU8030, Hitachi), and the structures of the CNTs were analyzed by a TEM (JEM2200-FS, JEOL). The functionalization, purity, and structural and chemical state of the CNTs were ascertained by FTIR (FT-IR spectrum 100, PerkinElmer, Inc.), X-ray photoelectron spectroscopy (XPS, Kratos, Shimadzu), EDS (JED2300-T, JEOL), TGA (DTG-60H, Shimadzu Scientific Instruments), Auger electron spectroscopy (AES) (JAMP-9500F, JEOL), and laser Raman spectroscopy (Lab RAM, HR-800, Horiba Jobin Yvon S.A.S.).

3. RESULTS AND DISCUSSION

Precise control over the size of NPs is crucial for the synthesis of CNTs of a uniform diameter as mentioned. Figure 1A shows a TEM image of core/shell $\text{Fe}/\text{Fe}_3\text{O}_4$ NPs deposited immediately from the particle/*n*-hexane solution on a TEM grid before the NPs were oxidized. The as-synthesized NPs, which were highly monodisperse and had core–shell structures, formed a hexagonal pattern via self-assembly (see also Figure S1 in the Supporting Information for TEM images of core/shell $\text{Fe}/\text{Fe}_3\text{O}_4$ NPs). The X-ray diffractogram of the core/shell $\text{Fe}/\text{Fe}_3\text{O}_4$ NPs shows no specific peak. In other words, the structures of the core/shell NPs were amorphous in nature (see

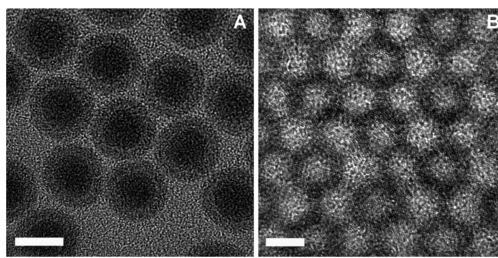


Figure 1. TEM images of catalytic NPs. (A) $\text{Fe}/\text{Fe}_3\text{O}_4$ core–shell NPs. (B) Hollow NPs after complete oxidation of the core particles. The HNPs were used as a catalyst for the growth of CNTs. The scale bars represent 5 nm.

Figure S2 in the Supporting Information for the XRD diffractogram of the amorphous core/shell NPs (ACS-NPs). A TEM image of NPs after complete oxidation of ACS-NPs is shown in Figure 1B. The NPs are highly monodisperse, forming self-assembled hexagonal patterns, and each NP possesses a spherical cavity at the center, surrounded by a shell composed of iron oxide. TEM images of HNPs show that the iron oxide shells are polycrystalline in nature (see also Figure S1 in the Supporting Information for low and high resolution TEM images of HNPs). The X-ray diffractogram of HNPs shows peaks, the positions and intensities of which coincided with those of Fe_3O_4 (JCPDS card number 88-0315); i.e., the shells of the HNPs were crystalline and composed of Fe_3O_4 ^{14,15} (see Figure S2 in the Supporting Information for the XRD diffractogram of the HNPs). The EDS spectrum shows that the stoichiometric ratio of Fe to O was 3:4, which also indicates a ferrite nature of Fe_3O_4 HNPs (see Figure S3 in the Supporting Information for the EDS spectrum of the HNPs). The final product, i.e., HNPs dispersed in *n*-hexane, were stable for months, whereas the ACS-NPs were unstable and highly susceptible to oxidation because oxygen could diffuse across the amorphous shells and the metallic cores were easily oxidized, which created a gap between the core and shell of NPs (see Figure S1 in the Supporting Information for TEM images of ACS-NPs). The FTIR spectrum of HNPs coated with oleic acid was exactly the same as that reported earlier⁴ (see Figure S3 in the Supporting Information for the FTIR spectrum). The diameters of Fe_3O_4 HNPs and cavity at the center were, respectively, 7.53 ± 0.11 and 4.02 ± 0.19 nm (see Figure S4 in the Supporting Information for the distribution of the diameter).

The formation of HNPs is based on the nanoscale Kirkendall effect.¹⁵ A single cavity is formed at the center of each ACS-NP via outward Fe diffusion across the amorphous spherical interface in the NPs. Trimethylamine *N*-oxide is an oxygen transfer reagent and the amount of oxidation of ACS-NPs depends on the volume ratio of trimethylamine *N*-oxide to the core/shell NPs and the temperature. Sufficient oxidation time and moderate temperature, i.e., 180 °C, are required for complete oxidation of each NP so that a cavity is formed at the center of the NP. Unlike the earlier reports,^{14,15} the addition of a small amount of oleic acid during the HNP synthesis worked efficiently to avoid agglomeration among ACS-NPs. Note that in the absence of oleic acid, a lot of aggregated NPs were observed.^{14,15}

HNPs capped with oleic acid formed a long-range, self-assembled monolayer on silicon substrates using a spin coating technique (see Figures S5 and S6 in the Supporting Information, respectively, for HRSEM and AFM images of

HNPs deposited on silicon substrates). This smooth surface would not have been formed if polydisperse NPs had been deposited on silicon substrates.

An ultradense forest of V-CNTs was grown after the PECVD process. Figure 2 shows SEM images of top and side views of a

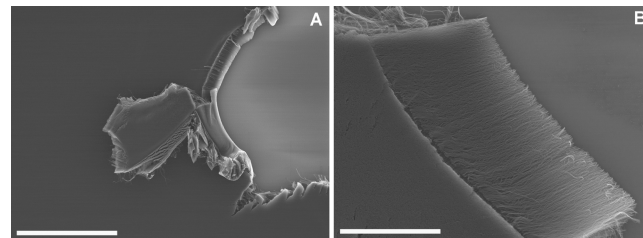


Figure 2. SEM images of CNTs. (A) Top view. CNTs are densely packed. The scale bar represents 100 μm. (B) Side view. The length of CNTs is uniform. The scale bar represents 10 μm.

forest of V-CNTs grown using monodisperse HNPs of 7.53 nm diameter on a silicon substrate (see also Figure S7 in the Supporting Information for an HRSEM image of a forest of V-CNTs). Closely packed CNTs grew vertically upward. The long ranged highly smooth top surface indicates a uniform growth rate of CNTs and monodispersity of catalytic NPs.^{1,4} The lengths of CNTs grown using HNPs of 7.53 nm diameter during the 10 and 20 min PECVD operation were, respectively, 10 and 20 μm. The catalytic activity of the NPs was high enough to produce these densely packed CNTs.

TEM images of CNTs are shown in Figure 3. Densely packed CNTs of a uniform diameter grew in bundles. Few NPs

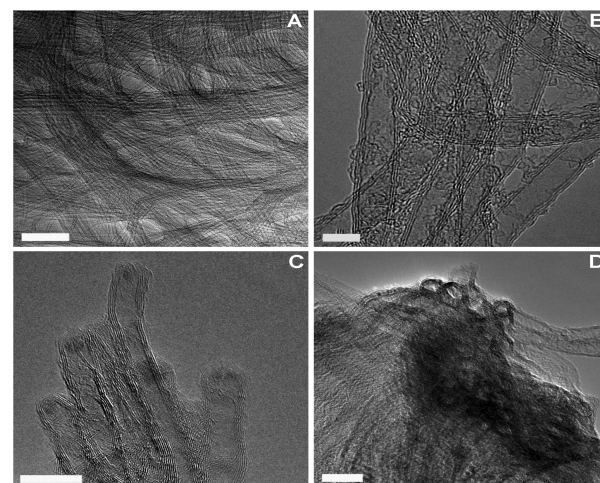


Figure 3. TEM images of CNTs. (A) Low resolution image of CNTs. The internal diameter of CNTs is uniform. The scale bar represents 50 nm. (B) High resolution image of CNTs. Most of the CNTs are triple-walled, and the internal diameter is uniform. The scale bar represents 5 nm. (C) NPs are trapped at the tip of CNTs. NPs are no longer hollow. The scale bar represents 10 nm. (D) A bundle of CNTs grew from densely packed NPs, and the other end of the CNTs is open-ended. The scale bar represents 10 nm.

were inactive according to the TEM observation, and the catalytic activity of the NPs was high as mentioned. The catalytic activity and actual state of NPs will be discussed in more detail later. The internal diameter and the number of walls of CNTs were measured from TEM images, targeting 947 CNTs. The internal diameter of CNTs grown using HNPs of

7.53 nm diameter was 4.86 ± 0.18 nm (see Figure S8 in the Supporting Information for the distribution of the internal diameter of CNTs). The average internal diameter of the CNTs was shorter than that of the catalytic HNPs, which was caused by shrinkage induced by the hollowness of the catalytic NPs and phase change in the NPs during the PECVD operation.^{4,15} NPs being trapped at the tip of individual CNTs, the growth of the CNTs was tip based and the other end of the CNTs was opened (see Figures 3C and 3D). No catalytic NPs were attached to the base of the CNTs. Dense bundles of open-end CNTs clearly suggest that CNTs grew from the densely packed self-assembled NPs. The catalytic HNPs were no longer hollow after the growth of the CNTs. The HNPs shrunk at elevated temperature and became solid spheres. The shrinkage was induced primarily by two causes: (a) collapse of the internal cavity and (b) phase change from iron oxide NPs to metallic ones in H_2 plasma. There were speculations in the past that iron oxide NPs may shrink without any evidence.^{1,11,16} In the present study, we confirmed by XPS analysis that NPs underwent a phase change during the H_2 plasma treatment¹⁷ (see Figure S9 for XPS analysis of NPs before and after the application of an H_2 plasma at 650°C) and the maximum size reduction caused by the phase change is found to be approximately 22.0% (see section 10 in the Supporting Information for a theoretical prediction of the reduction of the diameter of NPs). The diameter of NPs trapped at the tip of CNTs, which was measured targeting 32 NPs, was 4.91 ± 0.18 nm. The average diameter of NPs trapped at the tips of CNTs was close to that of the average internal diameter of CNTs.^{1,18}

The distribution of the number of walls of the V-CNTs is shown in Figure 4; 83.0% of the V-CNTs were triple-walled. To

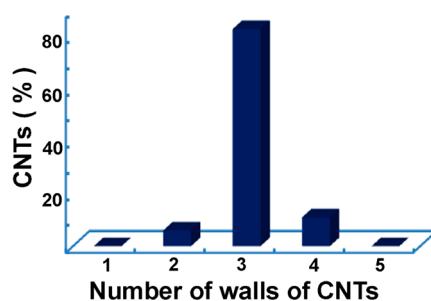


Figure 4. Distribution of the number of walls; 83% of the CNTs were triple-walled.

measure the areal density of CNTs, the mass gain method was employed.⁷ The mass gain method is valid for the estimation of the area density of highly pure CNTs. We therefore carried out TGA analysis of the as-synthesized CNTs to check the purity and structural stability of the CNTs (see Figure S10 in the Supporting Information for TGA of as-synthesized CNTs). The TGA result showed that the purity of CNTs was high; that is, the quantity of disordered carbon structures and catalytic NPs were, respectively, only 3.0 and 1.19 wt % of the total mass of the sample. Note that there were very few noticeable carbon impurities according to the TEM images as mentioned. The mass gain was measured, sampling randomly five areas of the forest of CNTs of $10\ \mu\text{m}$ length. The mass gain in each sample was 0.247, 0.262, 0.251, 0.219, and $0.239\ \text{mg cm}^{-2}$, from which the mass gain was estimated to be $0.243 \pm 0.016\ \text{mg cm}^{-2}$. The average mass of each TWNT of $10.0\ \mu\text{m}$ length being $39.8 \times$

$10^{-14}\ \text{mg}$, the area density of as-synthesized CNTs was estimated to be $0.6 \times 10^{12}\ \text{cm}^{-2}$, whereas the area density of the catalytic NPs was $2.5 \times 10^{12}\ \text{cm}^{-2}$, which was derived from the area density of mass of NPs, i.e., $0.00117\ \text{mg cm}^{-2}$, and the mass of each NP of 4.86 nm diameter, $4.68 \times 10^{-16}\ \text{mg}$. Therefore, the catalytic activity of the NPs was 24.0%. Note that the catalytic activity of the NPs estimated by the liquid-induced compaction method⁷ and TGA test was, respectively, 30.8% and 19.6% (see Figures S11 and S10 in the Supporting Information for the liquid-induced compaction test and TGA of as-synthesized CNTs).

The synthesis of TWNTs with such a large internal diameter is quite unusual,^{19,20} and furthermore the present area density, i.e., $0.6 \times 10^{12}\ \text{cm}^{-2}$, is the highest among TWNTs ever reported.^{19,20} Note that to date, the highest area densities of single-walled CNTs (SWNTs) and double-walled CNTs (DWNTs) are, respectively, 1.0×10^{12} and $1.5 \times 10^{13}\ \text{cm}^{-2}$.^{7,21,22} It is known that it is difficult to grow a forest of V-CNTs of internal diameters greater than 3.88 nm and that a possible solution is to increase the interparticle distance by reducing the concentration of NPs in the solvent.¹⁸ In the present case, limited nucleation sites on the monodisperse catalytic NPs of a uniform diameter induced the formation of mainly triple walls at an early stage of reaction. The mass flux of carbon around the NPs is expected to be quite low in the present case due to the relatively low operational temperature, which directly illustrates that the time spent on nucleation might have been longer than that in the case of higher temperature.⁴ Double- and triple-walled CNTs were previously grown using Fe_3O_4 NPs,⁴ whereas in the present case, triple-walled CNTs were obtained using catalytic Fe_3O_4 NPs of almost the same diameter as that of the previous ones.

The nucleation and growth mechanism of CNTs are so complex that they have not yet been fully understood. Let us discuss the nucleation and growth of CNTs based on the present experimental results (see also Figure 5). Monodispersity, hollowness, and polycrystallinity of the catalytic HNPs are the key factors for the growth of a dense forest of V-TWNTs of a uniform diameter. First of all, monodispersity and hollowness of the catalytic NPs are indispensable for avoiding agglomeration of NPs at elevated temperature.^{13,18} A wide gap between the nearest neighboring NPs in the self-assembled monolayer would reduce the chances of agglomeration up to some extent, but agglomeration eventually occurs once the interparticle potential becomes attractive due to the evaporation of oleic acid as the temperature rises.⁸ An alternative approach could be the employment of HNPs. The HNPs start to shrink due to the hollowness and phase transition from iron oxide to metallic iron in H_2 plasma with an increase in the temperature as mentioned. The activation energies along the polycrystalline boundaries are not the same throughout the NPs and hence the NPs start rearranging their shapes mainly from the most disoriented boundary caused by lattice mismatching. HNPs start to shrink toward the center of the cavity to form solid spheres. On the basis of the extra gap gained between the neighboring NPs after the shrinkage of the NPs, agglomeration of the NPs can be almost completely avoided. We speculate that there may be another important factor for avoiding agglomeration of NPs, i.e., friction against the movement of catalytic NPs on the silicon substrate at elevated temperature. Ligands immobilized on the surface of HNPs start to detach from the NPs and accumulate on the surface of the substrate once the temperature reaches 400°C , which could induce an

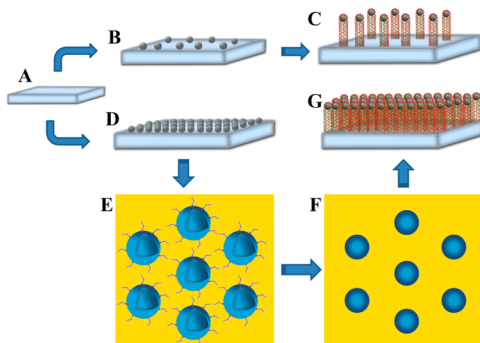


Figure 5. Schematic diagram of the synthesis of an ultradense forest of CNTs of a uniform diameter. A → B → C: Conventional approach. The interparticle distance should be long enough to avoid agglomeration among NPs. The area density of CNTs grown using the NPs as a catalyst decreases with an increase in the interparticle distance. A → D → E → F → G: Present approach. Hollow NPs modified with ligand are used as a catalyst. The diameters of the NPs and cavities are uniform. Densely packed HNPs are self-assembled on a substrate. HNPs shrink at elevated temperature via the collapse of the internal cavities and phase transition from iron oxide to metallic iron in H_2 plasma. Agglomeration of NPs is avoided on account of the shrinkage of the NPs and ligand attached to the NPs even at elevated temperature. Metallic iron NPs catalyze the growth of CNTs. Diffusion of the NPs into the substrate, which inactivates the growth of CNTs, is also avoided on account of the ligand. As a result, an ultradense forest of CNTs of a uniform diameter can be synthesized.

extra frictional force against the movement of NPs on the silicone substrate.²³ Note that NPs without any capping ligand start to slide as soon as the temperature reaches a certain level. TGA of the present HNPs modified with oleic acid is summarized in the Supporting Information (see Figure S12 for the TGA of conventional NPs and HNPs). In the case of the present HNPs, the weight loss curve is more complex; i.e., there was a very small amount of weight loss at around 230–400 °C due to oleic acid detached from the NPs, the weight loss continued even beyond 400 °C at a constant rate, and further weight loss beyond 400 °C was observed. The additional time delay, ranging from 60 to 90 s, was caused by the structural change from polycrystalline HNPs to single-crystalline solid ones. The time delay was in fact long enough to suppress the agglomeration even in the presence of H_2 plasma.

The establishment of barrier layers such as Al_2O_3 and SiO_2 on substrates is essential for the growth of CNTs^{2,24,25} because diffusion of catalytic NPs into the substrate matrix would be encouraged without any barrier layers, which would inactivate the catalytic NPs.^{7,26,27} We investigated inward diffusion of catalytic HNPs into a silicon matrix by SIMS and clarified that there was neither inward metallic diffusion nor formation of intermetallic compound at the interface of the silicon substrate (see Figure S13 in the Supporting Information for the SIMS analysis of the subsurface characterization). We suppose that inward diffusion of catalytic NPs was avoided on account of oleic acid attached to the surface of the NPs, which acted as a protecting layer during the 2 min preactivation period, which is much shorter than that in the case of the conventional CVD process.^{7,27,28}

The top of the carpet of the V-TWNTs was characterized using XPS, FTIR, and AES as mentioned (see Figures S14 and S15 and Tables S1 and S2 for the XPS analysis, Figure S16 for the FTIR spectrum, and Figure S17 for the AES analysis in the Supporting Information). According to the XPS, FTIR, and

AES analyses, it can be concluded that the iron oxide NPs underwent a phase change from Fe_3O_4 to metallic Fe and the growth of the V-CNTs was tip based. The absence of any peaks corresponding to iron carbide, i.e., $Fe2p$ and $C1s$, suggests that nucleation of CNTs started on metallic iron NPs. Fe NPs trapped at the tip of CNTs were protected from oxygen by the graphitic shells, and even after months in atmospheric conditions, no significant change was observed.^{29,30} The peak ratio of the sp^2 to sp^3 structures is an indicator of the structural stability of the CNTs. In the present case, those peaks were, respectively, 75.39% and 9.42% (see Figure S14 and Table S2 in the Supporting Information for the sp^2 and sp^3 peaks). Note that in the present XPS analysis, the top smooth surface of V-CNTs was systematically investigated, whereas in the case of the previous reports, randomly oriented CNTs were investigated.³¹ The top of the CNTs is very crystalline and composed of a hybrid structure of sp^2 and sp^3 bonded carbon.³²

The Raman spectrum of as-synthesized V-CNTs with 633 nm excitation wavelength is depicted in Figure 6. The G band

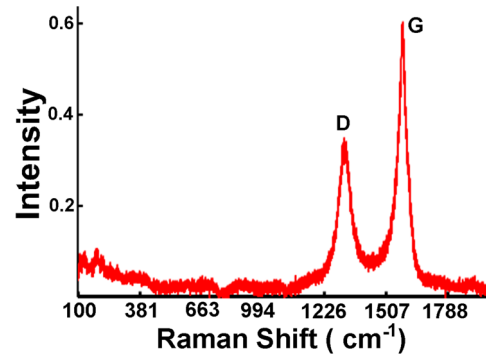


Figure 6. Raman spectrum of the as-synthesized CNTs. The ratio of the peak of the G band to that of the D band is 1.6.

represents the amount of graphitization associated with the V-CNTs, and the D band represents the amount of defects (mainly sp^2 defect and amorphous carbon). The ratio of the peak of the G band to that of the D band was 1.6. The FTIR, XPS, AES, and Raman studies showed that the quality of V-CNTs is very high and structurally stable.

The composition of catalytic NPs and the carbon–metal interaction during the growth of the CNTs have recently been debated.³³ It is extremely difficult to ascertain the actual state of the NPs during the growth of the CNTs without in situ studies.³⁴ In situ studies using XRD analysis help us to understand the detailed mechanism of nucleation of the CNTs but in fact failed to explain whether it was FeC or Fe_3C that catalyzed the growth of the CNTs.³⁵ Due to the complex nucleation and growth process, complementary characterization techniques are required to provide convincing evidence about the crystal structure and chemical state of the NPs. HRTEM, Fourier filtered HRTEM (FF-HRTEM), and point-localized EDS images of the NPs are shown in Figures S18 and S19 in the Supporting Information. The above images revealed the presence of five different crystal structures of NPs: (a) FeC (Figures S18A and S19A); (b) structurally disordered structure (see Figures S18B and S18C); (c) Fe_3C (Figures S18D, S18E, S18F, and S18G); (d) Fe_5C_2 (Figures S18H, S18I, S18J, and S18K); (e) iron oxide/iron carbide hybrid structure (Figures S18L and S19B). The active NPs trapped at the tip of the CNTs, which successfully initiated the growth of the CNTs,

were composed of FeC, which suggests that the NPs had undergone phase transition from the original ion oxide Fe_3O_4 to Fe and FeC, whereas the other four structures, i.e., disordered structure, Fe_3C , Fe_5C_2 , and iron oxide/iron carbide hybrid structure, were inactive. HRTEM images show that all of the inactive NPs are of the same size, which confirms that the inactivity of the NPs was not caused by the agglomeration. Although nucleation of the CNTs using Fe_3C NPs as a catalyst was previously confirmed by TEM and XRD analyses,³⁶ the present experiment showed that Fe_3C was inactive as in the case of refs 28 and 37. The existence of iron oxide/iron carbide NPs proved that not all of the iron oxide NPs were transformed into metallic Fe. Note that in the case of the inactive Fe_3C NPs, the number of graphitic layers established around the particles was greater than 4, whereas in the case of the inactive hybrid NPs composed of iron oxide/iron carbide, it was 2 or 3. The average diameter of both Fe_3C and iron oxide/iron carbide NPs was 5.50 nm. In the case of the active FeC NPs, on the other hand, triple-walled CNTs grew as mentioned and the average diameter of the NPs was 4.86 nm. In other words, there were two crucial differences between the active and inactive NPs: (a) the number of graphitic layers and (b) the size of NPs.

DWNTs and TWNTs are advantageous compared to SWNTs in terms of emission lifetime and durability because of their smaller curvatures and high current densities due to multiple metallic channels. TWNTs may well be utilized as mechanical and electronic elements, particularly, in complex nanobearing and nanogear-based devices.^{38,39}

4. CONCLUSIONS

We grew an ultradense forest of vertically aligned triple-walled carbon nanotubes of a uniform diameter using monodisperse hollow nanoparticles. The invincible coalescence among catalytic nanoparticles at elevated temperature was avoided by replacing the conventional solid catalytic nanoparticles with hollow ones. The monodisperse nanoparticles shrank on account of the hollowness and phase transition from iron oxide to pure iron, and consequently the interparticle distance increased. Eighty three percent of vertically aligned carbon nanotubes were triple-walled, and the internal diameter was 4.86 nm. The synthesis of triple-walled CNTs of such a high area density as $0.6 \times 10^{12} \text{ cm}^{-2}$ was achieved without any additional process. The purity of the present triple-walled CNTs was high. However, we will be thoroughly investigating the effect of the annealing conditions on the change and improvement in the structures of the triple-walled CNTs. We believe that the present approach may make a great contribution to the development of an innovative synthetic method for selective carbon nanotubes.

■ ASSOCIATED CONTENT

Supporting Information

TEM images of hollow nanoparticles (HNPs) and amorphous core/shell nanoparticles (ACS-NPs) (Figure S1); XRD analysis of HNPs and ACS-NPs (Figure S2); EDS and FTIR spectra of HNPs (Figure S3); distribution of the diameter of HNPs (Figure S4); HRSEM image of HNPs on a silicone substrate (Figure S5); AFM image and corresponding 3D plot of HNPs on a silicon substrate (Figure S6); HRSEM image of a forest of vertically aligned CNTs (Figure S7); distribution of the internal diameter of CNTs (Figure S8); XPS analysis of NPs before and after the application of a H_2 flow at 650 °C (Figure S9); TGA of as-synthesized CNTs (Figure S10); liquid-induced compac-

tion test of as-synthesized CNTs (Figure S11); reduction of the diameter of NPs via morphological change from an HNP to a solid NP and phase change caused by reduction with hydrogen plasma (theoretical calculation); TGA of conventional NPs and HNPs (Figure S12); SIMS study of the subsurface characterization of NPs supported on silicon substrates (Figure S13); XPS analysis of the top of the carpet of as-synthesized CNTs (Figures S14 and S15, Tables S1 and S2); FTIR spectrum of as-synthesized CNTs (Figure S16); AES of as-synthesized CNTs (Figure S17); HRTEM images of active and inactive NPs (Figure S18); point-EDS of active and inactive NPs (Figure S19). This material is available free of charge via the Internet at <http://pubs.acs.org>.

■ AUTHOR INFORMATION

Corresponding Author

maekawa@toyo.jp

Notes

The authors declare no competing financial interest.

■ ACKNOWLEDGMENTS

Part of this study has been supported by a Grant for the Program for the Strategic Research Foundation at Private Universities S1101017 organized by the Ministry of Education, Culture, Sports, Science and Technology (MEXT) since April 2011, and a Grant-in-Aid for Scientific Research, 24656148, organized by the Japanese Society for the Promotion of Science (JSPS), Japan, since April 2012.

■ REFERENCES

- (1) Lee, S. S.; Zhang, C.; Lewicka, Z. A.; Cho, M.; Mayo, J. T.; Yu, W. W.; Hauge, R. H.; Colvin, V. L. *J. Phys. Chem. C* **2012**, *116*, 10287–10295.
- (2) Patole, S. P.; Alegaonkar, P. S.; Shin, H.-C.; Yoo, J.-B. *J. Phys. D: Appl. Phys.* **2008**, *41*, 155311–155316.
- (3) Bower, C.; Zhu, W.; Jin, S.; Zhou, O. *Appl. Phys. Lett.* **2000**, *77*, 830–832.
- (4) Baliyan, A.; Fukuda, T.; Uchida, T.; Nakajima, Y.; Hanajiri, T.; Maekawa, T. *J. Mater. Chem.* **2012**, *22*, 5277–5282.
- (5) Baliyan, A.; Hayasaki, Y.; Fukuda, T.; Uchida, T.; Nakajima, Y.; Hanajiri, T.; Maekawa, T. *J. Phys. Chem. C* **2013**, *117*, 683–686.
- (6) Nessim, G. D.; Hart, A. J.; Kim, J. S.; Acquaviva, D.; Oh, J.; Morgan, C. D.; Seita, M.; Leib, J. S.; Thompson, C. V. *Nano Lett.* **2008**, *8*, 3587–3593.
- (7) Zhong, G.; Warner, J. H.; Fouquet, M.; Robertson, A. W.; Chen, B.; Robertson, J. *ACS Nano* **2012**, *6*, 2893–2903.
- (8) Bennett, R. D.; Hart, A. J.; Cohen, R. E. *Adv. Mater.* **2006**, *18*, 2274–2279.
- (9) Christen, H. M.; Puretzky, A. A.; Cui, H.; Belay, K.; Fleming, P. H.; Geohegan, D. B. *Nano Lett.* **2004**, *4*, 1939–1942.
- (10) Alvarez, N. T.; Li, F.; Pint, C. L.; Mayo, J. T.; Fisher, E. Z.; Tour, J. M. *Chem. Mater.* **2011**, *23*, 3466–3475.
- (11) Schäffel, F.; Kramberger, C.; Rümmeli, M. H.; Grimm, D.; Mohn, E.; Gemming, T. *Chem. Mater.* **2007**, *19*, 5006–5009.
- (12) Moodley, P.; Loos, J.; Niemantsverdriet, J. W.; Thüne, P. C. *Carbon* **2009**, *47*, 2002–2013.
- (13) Altavilla, C.; Sarno, M.; Ciambelli, P. *Chem. Mater.* **2009**, *21*, 4851–4858.
- (14) Peng, S.; Wang, C.; Xie, J.; Sun, S. *J. Am. Chem. Soc.* **2006**, *128*, 10676–10677.
- (15) Peng, S.; Sun, S. *Angew. Chem.* **2007**, *119*, 4233–4236.
- (16) Fu, Q.; Huang, S.; Liu, J. *J. Phys. Chem. B* **2004**, *108*, 6124–6129.
- (17) Hou, H.; Jun, Z.; Weller, F.; Greiner, A. *Chem. Mater.* **2003**, *15*, 3170–3175.

- (18) Baliyan, A.; Hayasaki, Y.; Fukuda, T.; Uchida, T.; Nakajima, Y.; Hanajiri, T.; Maekawa, T. *J. Nanopart. Res.* **2013**, *15*, 1693–1701.
- (19) Qin, H.; Shi, Z.; Gu, Z.; Qiu, J. *Chem. Commun.* **2007**, 1092–1094.
- (20) Flahaut, E.; Laurent, Ch.; Peigney, A. *Carbon* **2005**, *43*, 375–383.
- (21) Futaba, D. N.; Hata, K.; Yamada, T.; Hiraoka, T.; Hayamizu, Y.; Kakudate, Y.; Tanaike, O.; Hatori, H.; Yumura, M.; Iijima, S. *Nat. Mater.* **2006**, *5*, 987–994.
- (22) Zhong, G. F.; Iwasaki, T.; Kawarada, H. *Carbon* **2006**, *44*, 2009–2014.
- (23) Ayyappan, S.; Gnanaprakash, G.; Panneerselvam, G.; Antony, M. P.; Philip, J. *J. Phys. Chem. C* **2008**, *112*, 18376–18383.
- (24) Yamada, T.; Namai, T.; Hata, K.; Futaba, D. N.; Mizuno, K.; Fan, J.; Yudasaka, M.; Yumura, M.; Iijima, S. *Nat. Nanotechnol.* **2006**, *1*, 131–136.
- (25) Youn, S. K.; Yazdani, N.; Patscheider, J.; Park, H. G. *RSC Adv.* **2013**, *3*, 1434–1441.
- (26) Han, Z. J.; Ostrikov, K. *J. Am. Chem. Soc.* **2012**, *134*, 6018–6024.
- (27) Wang, Y.; Li, B.; Ho, P. S. *Appl. Phys. Lett.* **2006**, *89*, 183113–118115.
- (28) Jung, Y. J.; Wei, B.; Vajtai, R.; Ajayan, P. M.; Homma, Y.; Prabhakaran, K.; Ogino, T. *Nano Lett.* **2003**, *3*, 561–564.
- (29) Ghods, P.; Isgor, O. B.; Benesethaa, F.; Kingston, D. *Corros. Sci.* **2012**, *58*, 159–167.
- (30) Lee, D. W.; Yu, J. H.; Kim, B. K.; Jang, T. S. *F. J. Alloys Compd.* **2008**, *449*, 60–64.
- (31) Datsyuk, V.; Kalyva, M.; Papagelis, K.; Parthenios, J.; Tasis, D.; Siokou, A.; Kallitsis, I.; Galiotis, C. *Carbon* **2008**, *46*, 833–840.
- (32) Teo, K. B. K.; Chhowalla, M.; Amarasinghe, G. A. J.; Milne, W. I. *J. Vac. Sci. Technol. B* **2002**, *20*, 116–121.
- (33) Tessonniere, J. P.; Su, D. S. *Chem. Sus. Chem.* **2011**, *4*, 824–847.
- (34) Rodríguez-Manzo, J. A.; Terrones, M.; Terrones, H.; Kroto, H. W.; Sun, L.; Banhart, F. *Nat. Nanotechnol.* **2007**, *2*, 307–311.
- (35) Nishimura, K.; Okazaki, N.; Pan, L.; Nakayama, Y. *Jpn. J. Appl. Phys.* **2004**, *43*, L471–L474.
- (36) Yoshida, H.; Takeda, S.; Uchiyama, T.; Kohno, H.; Homma, Y. *Nano Lett.* **2008**, *8*, 2082–2086.
- (37) Lin, M.; Tan, J. P. Y.; Boothroyd, C.; Loh, K. P.; Tok, E. S.; Foo, Y. L. *Nano Lett.* **2006**, *6*, 449–452.
- (38) Cumings, J.; Zettl, A. *Science* **2000**, *289*, 602–604.
- (39) Fennimore, A. M.; Yuzvinsky, T. D.; Han, W. Q.; Fuhrer, M. S.; Cumings, J.; Zettl, A. *Nature* **2003**, *424*, 408–410.